

Nonspherical Pauli-forbidden states in deformed halo nuclei: Impact on the ${}^7\text{Be} + p$ resonant states in the particle rotor model

Shin Watanabe*

*National Institute of Technology (KOSEN), Gifu College, Motosu 501-0495, Japan and
RIKEN Nishina Center, Wako 351-0198, Japan*

Antonio M. Moro

*Departamento de Física Atómica, Molecular y Nuclear,
Universidad de Sevilla, Apartado 1065, E-41080 Sevilla, Spain*

(Dated: November 19, 2024)

Background: An important aspect of reducing nuclear many-body problems to few-body models is the presence of Pauli-forbidden (PF) states, which are excluded in fully antisymmetrized calculations. Insufficient treatments of PF states in deformed halo nuclei underscore the need for model refinement.

Purpose: We propose a new method utilizing Nilsson states as PF states in the orthogonality condition model, and investigate the impact of PF states on the properties of resonant states.

Method: We investigate the scattering states of ${}^8\text{B}$ within the particle rotor model (PRM) framework based on a deformed ${}^7\text{Be}$ core and p two-body model. We compare several methods for eliminating PF states and test them with the experimental data.

Results: Our model successfully reproduces the experimental excitation function for elastic scattering cross section by properly eliminating PF states. The same calculation predicts the presence of a low-energy bump in the inelastic scattering excitation function, although its position is overestimated by about 1 MeV compared to experimental data.

Conclusion: This study extends the applicability of the PRM, offering a comprehensive approach for exploring structures and reactions of loosely bound nuclei such as ${}^8\text{B}$. Future integration with the continuum discretized coupled channels method promises to further advance the research.

I. INTRODUCTION

Beyond the conventional picture of spherical halos, recent experiments have revealed the existence of deformed halo nuclei [1–5]. They are characterized not only by their extended neutron distributions but also by the deformation of their core. An accurate description of deformed halo nuclei is a frontier in modern nuclear physics, integrating state-of-the-art models to elucidate the complex interplay between a valence nucleon and a deformed core [6–11]. In the context of few-body models, the continuum discretized coupled channels (CDCC) method has been significantly developed [12–15]. Originally, CDCC was designed to describe reactions involving a deuteron and a target nucleus (T), based on the $p + n + T$ three-body model. Recently, CDCC has been extended to include core excitation effects, leading to the extended version of CDCC (XCDCC) [16–20]. For example, XCDCC has been applied to ${}^{11}\text{Be}$ scattering in the ${}^{10}\text{Be} + n + T$ three-body model with ${}^{10}\text{Be}$ core excitation, revealing significant interference between the valence and core excitations in the breakup reactions [21–23]. Additionally, the inclusion of core excitation has been successfully achieved using the exact Faddeev formalism, which has already been applied to all relevant reaction channels

such as elastic, inelastic, transfer, and breakup [24, 25]. These efforts to accurately represent many-body systems through few-body models are a foundational task, enabling us to interpret complicated phenomena from a simple perspective.

When reducing many-body problems to few-body models, we often encounter the challenge of handling Pauli-forbidden (PF) states, especially for deformed nuclei. The PF states are automatically excluded from the many-body wave function through antisymmetrization, yet they require deliberate exclusion in few-body approaches. The problem becomes more involved when considering deformation effects, such as in the Nilsson model [26, 27] or in the particle rotor model (PRM) [28–30]. Consider ${}^8\text{B}$ in a ${}^7\text{Be} + p$ two-body model as an example. In the spherical shell model, the last proton occupies the $0p_{3/2}$ orbital, which can accommodate up to four protons. Consequently, there is no need for special treatment to eliminate PF states as long as we consider p -wave states. However, when considering deformation, the $0p_{3/2}$ orbital splits into the $[110\ 1/2]$ and $[101\ 3/2]$ Nilsson orbitals,¹ which can accommodate up to two protons, respectively. Therefore, the $[110\ 1/2]$ orbital becomes forbidden, as it is already filled by two protons in

* s-watanabe@gifu-nct.ac.jp; This work was conducted during a sabbatical leave at the Departamento de Física Atómica, Molecular y Nuclear, Universidad de Sevilla.

¹ We consider the Nilsson orbital labeled by $[Nn_3\Lambda\ \Omega]$ throughout this paper, where N is the principal quantum number denoting the major shell, n_3 is the number of nodes along the z' axis (symmetry axis), and Λ (Ω) is the projection of the angular momentum (total angular momentum) onto the z' axis.

the deformed ${}^7\text{Be}$ core, necessitating careful treatment of PF states.

In this study, we focus on the refinement of the projectile wave function of deformed halo nuclei using the PRM for further applications within the XCDCC reaction framework. We demonstrate various treatments for excluding the PF states and investigate their impact on the resonant-state properties. Previous research presented a simple method to eliminate PF states in the deformed halo nucleus ${}^{31}\text{Ne} = {}^{30}\text{Ne} + n$ [29, 30]. In these works, the PF states are obtained as bound states, and eliminated after solving the Schrödinger equation. Due to its simplicity, this technique has been widely used in many studies [22, 31–33]. However, as will be shown later, we find that this method cannot be directly applied to ${}^8\text{B} = {}^7\text{Be} + p$, where the PF state emerges as a resonant state, complicating its exclusion. To overcome this limitation, we propose using the Nilsson model to represent PF states in the orthogonality condition model (OCM) [34–36]. This method enables us to exclude the PF states before solving the Schrödinger equation. This approach not only overcomes the limitations encountered in ${}^8\text{B}$ calculation but also offers the way for broader applications. Integrating the projectile wave functions calculated from this method with commonly used reaction frameworks, such as the XCDCC method (for breakup), and the distorted-wave Born approximation (DWBA) and the adiabatic distorted-wave approximation (ADWA) [37] (for transfer reactions), could significantly improve our understanding and predictive capabilities in nuclear physics.

This paper is organized as follows. In Sec. II, we first explain the PRM framework without considering the PF states. This section is divided into three subsections, each explaining a different method for treating PF states. Section II A provides a brief review of the treatment outlined in Refs. [29, 30]. In Sec. II B, we show the standard OCM using spherical PF states for comparison. In Sec. II C, we propose a new method using deformed PF states in the OCM. Section III presents the results obtained from these different models. Finally, the paper concludes in Sec. IV.

II. FORMULATION

We consider the scattering states of ${}^8\text{B} = {}^7\text{Be} + p$ using the two-body Hamiltonian with core excitation defined as

$$H_1 = T_{\mathbf{r}} + V(\mathbf{r}, \boldsymbol{\xi}) + h_{\text{core}}(\boldsymbol{\xi}), \quad (1)$$

where \mathbf{r} denotes the coordinate between proton and the core, and $\boldsymbol{\xi}$ is the internal coordinate of the core, i.e., direction of the symmetry axis of the deformed core. The operator $T_{\mathbf{r}}$ represents the kinetic energy and h_{core} is the internal Hamiltonian, governing the degree of freedom of the core: $(h_{\text{core}} - \epsilon_I)\phi_I = 0$, where ϕ_I is the rotational wave function with the core spin I , and ϵ_I is the corresponding eigenenergy. In this study, an effective potential

V is assumed to be

$$V(\mathbf{r}, \boldsymbol{\xi}) = V_{\text{def}}(\mathbf{r}, \boldsymbol{\xi}) + V_{\ell s}(r)\boldsymbol{\ell} \cdot \mathbf{s} + V_{\text{Coul}}(r), \quad (2)$$

where V_{def} is a deformed potential, $V_{\ell s}$ is the spin-orbit interaction with the angular momentum $\boldsymbol{\ell}$ and proton spin $\mathbf{s} = 1/2$, and V_{Coul} is the Coulomb interaction. For simplicity, both $V_{\ell s}$ and V_{Coul} are treated as spherical potentials.

The total wave function of the ${}^7\text{Be} + p$ system, Ψ_{JM} , is expanded as

$$\Psi_{JM}(\mathbf{r}, \boldsymbol{\xi}) = \sum_c \frac{u_c(r)}{r} \Phi_{c, JM}(\hat{\mathbf{r}}, \boldsymbol{\xi}) \quad (3)$$

with

$$\Phi_{c, JM}(\hat{\mathbf{r}}, \boldsymbol{\xi}) = [\mathcal{Y}_{\ell j}(\hat{\mathbf{r}}) \otimes \phi_I(\boldsymbol{\xi})]_{JM}, \quad (4)$$

where J and M denote the total angular momentum of the system and its z component, respectively, j is the total angular momentum combining $\boldsymbol{\ell}$ and \mathbf{s} . The function $\Phi_{c, JM}$ is the direct product of the spin-angular function $\mathcal{Y}_{\ell j m_j}$ and the core wave function $\phi_{I m_I}$, where m_j (m_I) is the z component of j (I), and c indicates the channel $c = \{\ell j I\}$. The function u_c describes the relative motion between the proton and the core in the c channel, and the set of u_c is obtained by solving a set of coupled-channel equations

$$[T_{r\ell} - \epsilon_I]u_c(r) + \sum_{c'} V_{cc'}(r)u_{c'}(r) = 0 \quad (5)$$

under the appropriate boundary conditions. Here, $T_{r\ell}$ denotes the kinetic energy, $V_{cc'}(r) = \langle \Phi_{c, JM} | V | \Phi_{c', JM} \rangle$ is the coupling potential, and ϵ_I is the relative energy defined as $\epsilon_I = \epsilon - \epsilon_I$, with ϵ being the total energy.

At this stage, the presence of PF states is not taken into account.

A. Model I: Standard PRM

A simple method to eliminate the forbidden states in deformed halo nuclei is outlined in Refs. [29, 30]. We refer to this method as the “standard PRM (std-PRM)” to distinguish it from the models described later. First, we introduce the Nilsson Hamiltonian by omitting h_{core} from Eq. (1) as

$$H_{\text{Nil}} = T_{\mathbf{r}} + V(\mathbf{r}, \boldsymbol{\xi}). \quad (6)$$

By solving the Schrödinger equation with H_{Nil} , using the same form of wave functions [Eq. (3)], we can conduct Nilsson model calculations within the PRM framework. In this calculation, several states with different J values, but having the same value of Ω , become energetically degenerate if the model space $\{\ell j I\}$ is sufficiently large. Here, Ω denotes the projection of the total angular momentum onto the z' axis in the body-fixed frame.

The anticipated behavior is schematically illustrated in Fig. 1(a), in which the deformation parameter β_2 varies from 0 to a specific value $\bar{\beta}_2$. Note that each Nilsson orbital is doubly degenerate due to time-reversal symmetry. Following the standard procedure, we allocate two protons to each Nilsson orbital starting from the lowest-energy level, enabling us to identify the Nilsson orbital that accommodates the last unpaired proton. Consequently, the $[000\ 1/2]$ and $[110\ 1/2]$ Nilsson orbitals are considered as the PF states. In Fig. 1, PF states are represented by the filled circles, while the last proton is indicated by the open circle for further explanation.

Subsequently, by gradually increasing the value of core excitation energies to the physical ones, we can track the evolution of the Nilsson states. For convenience, we introduce αh_{core} to H_{Nil} , where $\alpha = 0$ corresponds to the Nilsson model and $\alpha = 1$ denotes the PRM. This evolution is shown in Fig. 1(b). At this stage, Ω is no longer a good quantum number, and each Nilsson orbital splits into two states. Through this process, we can identify the states originating from the $[000\ 1/2]$ and $[110\ 1/2]$ Nilsson orbitals. These states, indicated as “(I) std-PRM” in Fig. 1(b), are interpreted as PF states, and subsequently excluded after solving the Schrödinger equation with H_1 . The next-lowest-energy state, shown by the open circle in Fig. 1(b), is then considered as the lowest-energy state in Model I.

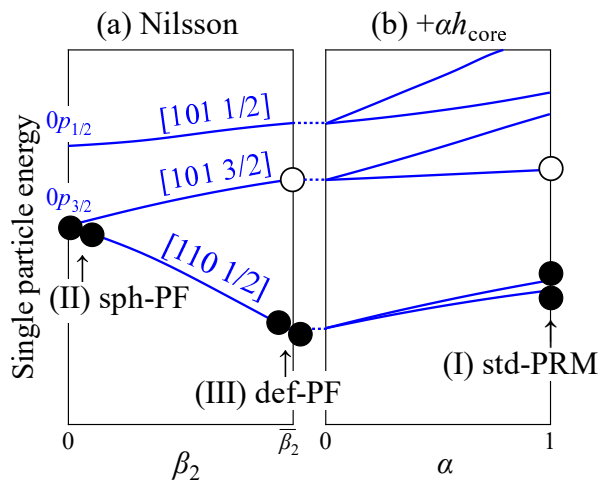


FIG. 1. Schematic illustration of the evolution of the single particle energy by incorporating (a) deformation and (b) core excitation. (a) corresponds to the Nilsson diagram, where the deformation parameter β_2 increases from 0 to a specific value $\bar{\beta}_2$. (b) demonstrates the energy splitting by adding αh_{core} to H_{Nil} , where $\alpha = 0$ corresponds to the Nilsson model and $\alpha = 1$ represents the PRM. The filled circles denote the PF states while the open circle indicates the last proton. Arrows labeled (I) std-PRM (standard PRM), (II) sph-PF (spherical PF states), and (III) def-PF (deformed PF states) are shown to explain various treatments of PF states. See text in detail.

B. Model II: Spherical PF model

Another way of eliminating PF states is to introduce a Pauli blocking operator to Eq. (1), which is known as the orthogonality condition model (OCM) [34–36]. The Hamiltonian is defined as

$$H_2 = T + V + h_{\text{core}} + V_{\text{PF}} \quad (7)$$

with

$$V_{\text{PF}} = \sum_{i=1}^{N_{\text{PF}}} \lambda_i |\bar{\Psi}^{(i)}\rangle \langle \bar{\Psi}^{(i)}|, \quad (8)$$

where the operator form is adopted for notational simplicity. In Eq. (8), $\bar{\Psi}^{(i)}$ represents the i th PF state and N_{PF} is the total number of PF states. In practice, $\lambda_i = 10^6$ MeV is chosen to ensure convergence.

In the standard OCM, spherical PF (sph-PF) states are used to define $\bar{\Psi}^{(i)}$ in Eq. (8). Therefore, in addition to our proposed model using the deformed PF (def-PF) states shown in the next subsection, we also conduct calculations using the sph-PF states. These sph-PF states (for given J and M) can be explicitly defined using the same form as Eq. (3):

$$\bar{\Psi}_{JM}^{(i)}(\mathbf{r}, \boldsymbol{\xi}) = \sum_c \frac{g_c^{(i)}(r)}{r} \Phi_{c, JM}(\hat{\mathbf{r}}, \boldsymbol{\xi}), \quad (9)$$

where $g_c^{(i)}$ is the radial wave function. Once $\bar{\Psi}_{JM}^{(i)}$ is determined, the set of coupled-channel equations for u_c is derived as follows:

$$[T_{r\ell} - \varepsilon_I]u_c(r) + \sum_{c'} V_{cc'}(r)u_{c'}(r) + \sum_{c'} \int dr' W_{cc'}(r, r')u_{c'}(r') = 0, \quad (10)$$

where $W_{cc'}(r, r')$ is the non-local potential defined as

$$W_{cc'}(r, r') = \sum_{i=1}^{N_{\text{PF}}} \lambda_i g_c^{(i)}(r) g_{c'}^{(i)*}(r'). \quad (11)$$

These non-local coupled-channel equations are solved under the same boundary condition as for Eq. (5). The R -matrix code available in Refs. [38, 39] is utilized.

In the actual ${}^7\text{Be} + p$ calculation of the sph-PF model, the sph-PF states, equivalent to two $0p_{3/2}$ states, are determined in the Nilsson model by setting $\beta_2 = 0.0001$ instead of zero. This minimal β_2 is necessary to avoid possible configuration mixing of the four $0p_{3/2}$ states, which could occur at $\beta_2 = 0$ due to the degeneracy of $\epsilon_I = 0$, as described by $[\mathcal{Y}_{p3/2} \otimes \phi_I]_{JM}$. Introducing a small β_2 value effectively resolves this degeneracy and aligns the states, allowing for a reasonable definition of sph-PF states corresponding to two $[110\ 1/2]$ Nilsson states in the spherical limit. These well-defined states are then employed as the PF states in Eq. (8), which are indicated as “(II) sph-PF” in Fig. 1.

C. Model III: Deformed PF model

As a novel approach, we propose using def-PF states in the OCM, which we call the def-PF model. In this model, we assume that $\bar{\Psi}^{(i)}$ in Eq. (8) should be deformed rather than spherical. A natural choice is to use the i th Nilsson state, which is indicated by “(III) def-PF” in Fig. 1. As discussed in Sec. II A, the Nilsson state (for given J and M) can be obtained by solving the Schrödinger equation with H_{Nil} within the PRM framework. Therefore, the Nilsson states $\bar{\Psi}_{JM}^{(i)}(\mathbf{r}, \boldsymbol{\xi}) \equiv \langle JM; \mathbf{r}, \boldsymbol{\xi} | \bar{\Psi}^{(i)} \rangle$ are explicitly defined in Eq. (9). Once $\bar{\Psi}_{JM}^{(i)}$ is determined, the set of coupled-channel equations (10) is solved in the same way as described in Sec. II B.

III. RESULTS

A. Model setting and structure analysis

In the actual calculation, we start with the potential parameters for the spherical model shown in Ref. [40]. For simplicity, the core-spin orbit interaction, i.e., V_{LI} in Ref. [40], is neglected. For the deformed potential V_{def} , we adopt the deformed Woods-Saxon potential with radius $R_0 = 2.391$ fm and diffuseness $a_0 = 0.535$ fm. The depth of this deformed Woods-Saxon potential, denoted as V_{def}^0 , will be determined later. The Woods-Saxon volume type is employed for $V_{\ell s}$, with a depth $V_{LS}^0 = -7$ MeV, and the same radius $R_0 = 2.391$ fm and diffuseness $a_0 = 0.535$ fm. Regarding the core state, we consider the negative-parity states from $I^\pi = 1/2^-$ to $13/2^-$ to clearly define the PF states. For the energies ϵ_I corresponding to these states, we use the experimental data for the four lowest-energy states ($\epsilon_{3/2} = 0$ MeV, $\epsilon_{1/2} = 0.43$ MeV, $\epsilon_{7/2} = 4.57$ MeV, and $\epsilon_{5/2} = 6.73$ MeV). For the higher-energy states, we use extrapolated values using the formula [41, 42]:

$$\epsilon_I = \epsilon^0 + A \left[I(I+1) + a(-)^{I+1/2}(I+1/2) \right], \quad (12)$$

where the constants (ϵ^0 , A , and a) are determined from the three lowest experimental energies: $\epsilon^0 = -0.564$ MeV, $A = 0.486$ MeV, and the decoupling factor $a = -1.29$. The deformation parameter β_2 is set to 0.586.

First, we solve the Schrödinger equation using H_{Nil} to define the PF states. Figure 2(a) presents the Nilsson diagram obtained within the PRM framework. The resonant energies indicated by the dotted lines are estimated using the complex scaling method [43, 44]. In the standard Nilsson model [26, 27], each orbital is doubly degenerate. In contrast, in our calculations, the number of Nilsson states depends on J^π and the model space $\{\ell j I\}$. For example, for $J^\pi = 0^+$, only one state is obtained for the $[110\ 1/2]$ Nilsson orbital because only the $[\mathcal{Y}_{p3/2} \otimes \phi_{3/2}]_{0^+}$ configuration is allowed with $p_{3/2}$. Note

that the energies corresponding to a specific Nilsson orbital are degenerate for different J^π . This degeneracy allows us to identify which state corresponds to which Nilsson orbital. Consequently, states up to the $[110\ 1/2]$ orbital are considered as the PF states in Model III. For the negative-parity states ($J^\pi = 1^-$ and 2^-), the $[000\ 1/2]$ Nilsson states are regarded as the PF states.

On the other hand, in Model I, we further trace how the Nilsson states evolve by adding αh_{core} to H_{Nil} . Figures 2(b)–2(e) illustrate the energy splitting for $J^\pi = 0^+$ to 3^+ , respectively. This procedure enables us to identify the states originating from the $[110\ 1/2]$ Nilsson orbital, which are considered to be PF states. Subsequently, the PF states are extracted after solving the Schrödinger equation with H_1 . However, for the $J^\pi = 3^+$ state, one of the PF states significantly increases in energy and approaches the next energy level in the continuum region. This situation makes it difficult to unambiguously identify the PF state from the solution. We therefore show the results without excluding this PF state in Model I.

Next, we determine the potential depth V_{def}^0 for each J^π configuration through the following procedure. For the $J^\pi = 2^+$, 1^+ , and 3^+ states, V_{def}^0 is adjusted to the experimentally well-established bound and resonant energies: $\epsilon_{\text{gs}}(2_1^+) = -0.137$ MeV ($E_x = 0$ MeV), $\epsilon_{\text{res}}(1_1^+) = 0.63$ MeV ($E_x = 0.77$ MeV), and $\epsilon_{\text{res}}(3_1^+) = 2.18$ MeV ($E_x = 2.32$ MeV). As for the 3^+ states in Model I, we assume that the 3_1^+ state corresponds to the PF state and that the 3_2^+ state is the physical one, which is adjusted to the experimental data. For the $J^\pi = 0^+$, 1^- , and 2^- states, V_{def}^0 is tuned so as to reproduce the phase shift calculated by the ab initio no-core shell model/resonating group method (NCSM/RGM) [10]. Figures 3(a) $J^\pi = 0^+$, 3(b) $J^\pi = 1^-$, and 3(c) $J^\pi = 2^-$ display the resultant phase shifts. The solid lines represent the results of the def-PF model, which fairly reproduce the NCSM/RGM calculations shown by the dot-dashed lines. Note that the results of the std-PRM are almost identical. Similarly, the sph-PF model (dashed line) yields almost the identical phase shifts for the 1^- and 2^- states. For the 0^+ state, the resultant resonant energy $\epsilon(0_1^+) \approx 1.1$ MeV is somewhat lower than the NCSM/RGM calculation $\epsilon(0_1^+) \approx 2.8$ MeV. However, adjusting this resonance by simply reducing V_{def}^0 is impractical as the sph-PF state becomes unbound before reaching the proper position of the 0_1^+ resonance. This result supports the use of the Nilsson state as the PF state. Furthermore, since the 0^+ state does not significantly impact the elastic and inelastic cross sections, we have maintained the same potential for the 0^+ state as used in the other models. The determined V_{def}^0 values are summarized in Table I. It is interesting to note that the obtained parameters remain almost constant for all J^π states, contrasting with the spherical model [40], where the potential depths are shallower for the positive-parity states ($V^0 \approx 40$ MeV) and deeper for the negative-parity states ($V^0 \approx 60$ MeV). This improvement can be understood from the single-particle energy in the Nilsson model. With deforma-

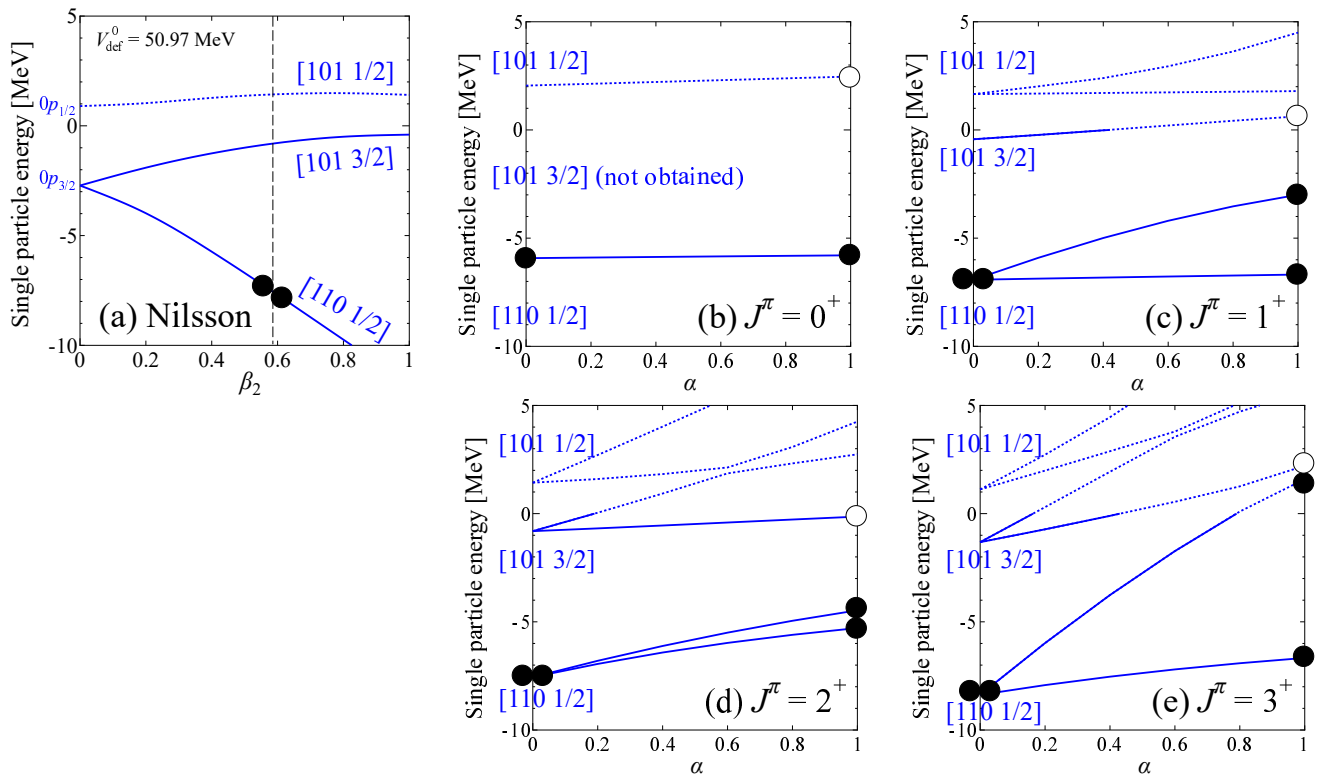


FIG. 2. Single particle energy used to define the forbidden states within the PRM framework. (a) displays the Nilsson diagram, where the $[110\ 1/2]$ Nilsson orbital is occupied by two protons, represented by the filled circles. The value $\beta_2 = 0.586$ is indicated by the dashed line. (b)–(e) illustrate the energy splitting as α varies from 0 (Nilsson) to 1 (std-PRM) for the $J^\pi = 0^+$ to 3^+ states, respectively, with $\beta_2 = 0.586$. Note that the potential depths of V_{def} are optimized for each J^π as summarized in Table I.

tion, the $[101\ 3/2]$ Nilsson state increases in energy for the positive-parity states (requiring a deeper potential to obtain the same eigenenergy), while the $[220\ 1/2]$ Nilsson state decreases for negative-parity states (requiring a shallower potential to achieve the same eigenenergy).

TABLE I. Potential depth parameters, V_{def}^0 in MeV, used in the calculations.

J^π	Model I (std-PRM)	Model II (sph-PF)	Model III (def-PF)
0^+	48.00	48.00	48.00
1^+	49.83	49.23	48.70
2^+	50.97	50.72	50.41
3^+	52.41	50.61	49.98
1^-	48.00	48.00	48.00
2^-	53.00	53.00	53.00

Next, we compare the eigenphases calculated with Model I (std-PRM) and Model III (def-PF). Figure 4 illustrates the eigenphases for the (a) $J^\pi = 2^+$, (b) $J^\pi = 1^+$, and (c) $J^\pi = 3^+$ states. The solid and dotted lines represent the def-PF model and the std-PRM, respectively. Unlike the phase shifts for $J^\pi = 0^+$, 1^- , and 2^- depicted in Fig. 3, V_{PF} alters the resonant energies

and widths. Furthermore, for the 3^+ state in the std-PRM [dotted line in Fig. 4(c)], an additional resonance emerges at around $\varepsilon \approx 1.6$ MeV, which can be regarded as the PF state. This resonance cannot be eliminated by changing V_{def}^0 if the neighboring 3^+ resonant state is correctly positioned. For comparison, the NCSM/RGM calculations [10] are also shown by the dashed lines. It should be noted that the potential depths are adjusted to the experimental ground and resonant energies in our calculations (both std-PRM and def-PF), whereas no phenomenological correction has been applied in the NCSM/RGM. For the resonances with a narrow width ($J^\pi = 1^+$ and 3^+), the observed behaviors are almost identical. However, for the resonances with a broader width, the present models do not exhibit the similar behavior regardless of the inclusion of V_{PF} .

We analyze the components of the ${}^8\text{B}$ wave functions in terms of core and proton states. Table II displays the probabilities of $[I^\pi \otimes (\ell j)]$ configurations in the wave functions for the (a) $J^\pi = 2^+$ ground state, (b) $J^\pi = 1^+$ resonant state, and (c) $J^\pi = 3^+$ resonant state using the std-PRM and the def-PF model. Note that only main components are listed in the tables, with the largest two components highlighted in bold. For the 2^+ ground state and the 1^+ resonant state, the largest two components are the same although their values slightly differ. How-

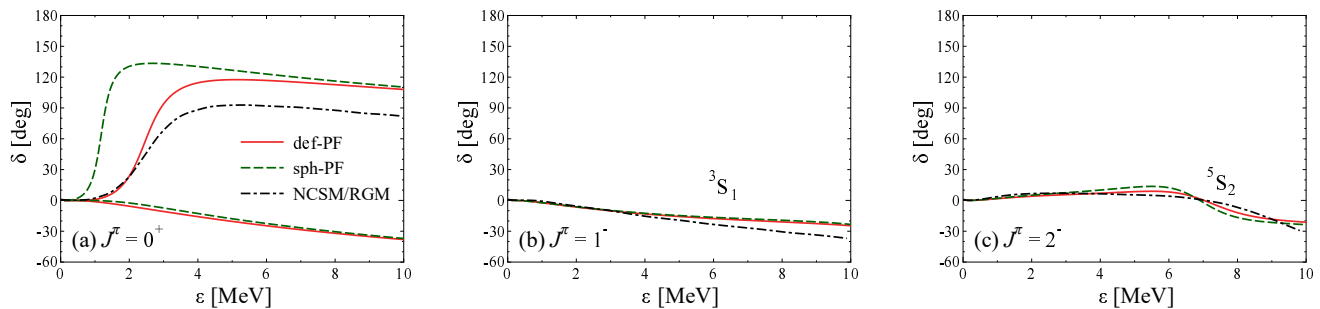


FIG. 3. Eigenphase shift for $J^\pi = 0^+$, and diagonal phase shifts for $J^\pi = 1^-$ and 2^- in the channel-spin representation. The solid and dashed lines represent Model III (def-PF) and Model II (sph-PF), while the dot-dashed line corresponds to the ab initio NCSM/RGM calculation [10]. It should be noted that Model I (std-PRM) aligns with the solid line for these J^π .

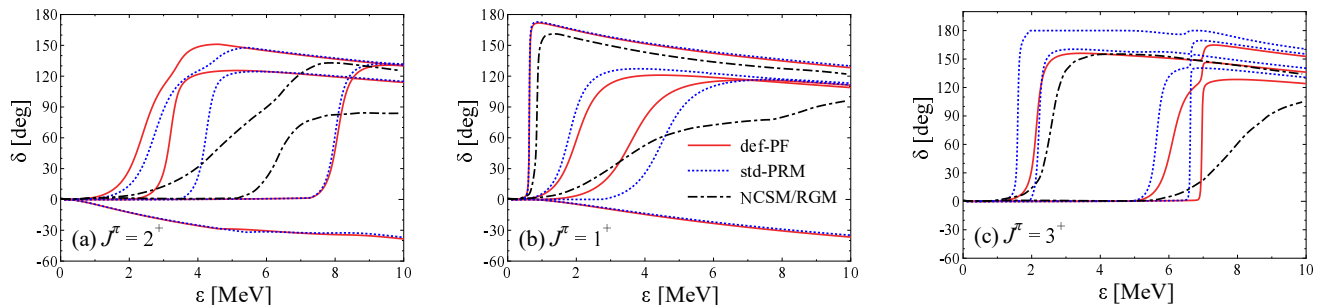


FIG. 4. Eigenphase shifts for $J^\pi = 2^+$, 1^+ , and 3^+ . The solid and dotted line represent Model III (def-PF) and Model I (std-PF), while the dot-dashed line corresponds to the ab initio NCSM/RGM calculation [10].

ever, for the 3^+ resonant state, the two dominant components change significantly compared to those of the 2^+ and 1^+ states. This difference may arise from the avoided crossing in the continuum region. In Fig. 2 (e), the 3^+ resonant state of interest, indicated by the open circle, is significantly approached by the PF state originating from the $[110\ 1/2]$ Nilsson state. This proximity leads to a notable exchange of their main components around $\alpha \approx 1$. Thus, the 3^+ resonant state is strongly affected by the PF state, highlighting the importance of adopting alternative approaches to effectively exclude PF states.

Following the analysis of physical states, we further investigate the components of the ^8B wave functions for the PF states. Table III presents the main configurations $[I^\pi \otimes (\ell j)]$ for the PF states of the (a) $J^\pi = 2^+$, (b) $J^\pi = 1^+$, and (c) $J^\pi = 3^+$ in the Nilsson model and the std-PRM. The lowest and the second-lowest positive-parity PF states are represented as PF1 and PF2, respectively. These states, PF1 and PF2, correspond to the two leftmost states (Nilsson) and the two rightmost states (std-PRM) states depicted by the filled circles in Figs. 2(c)–2(e). In the Nilsson model calculations, the small value of $\alpha = 0.0001$ is used to effectively resolve the degeneracy of the two $[110\ 1/2]$ Nilsson states at $\alpha = 0$; the same technique is used to define the sph-PF states (see Sec. II B in detail). Table III highlights that incorporating core excitations ($\alpha = 1$) generally leads to a reduction in the high- I components across all the PF states. Notably, the PF1 state in $J^\pi = 1^+$ remains almost un-

changed between the Nilsson model and the std-PRM, likely due to its minimal high- I components. Conversely, the significant energy rise for the PF2 state in $J^\pi = 3^+$ can be attributed to the high proportion (0.688) of the $[9/2^- \otimes p_{3/2}]$ configuration, with $\epsilon_{9/2} = 14.6$ MeV, resulting in its emergence in the continuum region. This situation underscores the necessity for developing methods to effectively exclude PF states from continuum region.

B. Application to the $p + ^7\text{Be}$ reaction

As a test of the developed models, we have computed excitation functions for the elastic and inelastic cross sections for the $p + ^7\text{Be}$ reaction, and compared with the existing experimental data [46]. Figure 5 shows the excitation function of the $p + ^7\text{Be}$ elastic scattering cross section at 123° . Figure 5(a) compares three models, while Fig. 5(b) illustrates the J^π contributions by expanding the model space for our best result, the def-PF model. In Fig. 5(a), the dotted and solid lines represent the results of the PRM and def-PF model, respectively. Both models exhibit similar behavior in the low-energy region ($\epsilon \lesssim 1.3$ MeV) and predict the 1_1^+ resonance at $\epsilon = 0.63$ MeV, in agreement with the experimental data [46]. Above this energy region, the def-PF model well reproduces the second peak, mainly attributed to the 3^+ resonance at $\epsilon = 2.18$ MeV. On the contrary, as discussed in Fig 4, the PRM predicts an additional peak at around $\epsilon \approx 1.6$

TABLE II. The probability of $[I^\pi \otimes (\ell j)]$ in the ${}^8\text{B}$ wave functions for the (a) $J^\pi = 2^+$ ground state, (b) $J^\pi = 1^+$ resonant state, and (c) $J^\pi = 3^+$ resonant state using the std-PRM and the def-PF model. Only main components are listed in the tables, and the largest two components are shown in bold. Note that the probabilities for the resonant states are estimated as those of pseudostates using the Gaussian expansion method [45].

(a) $J^\pi = 2^+$ ground state

Model	ε (MeV)	$[3/2^- \otimes p_{1/2}]$	$[3/2^- \otimes p_{3/2}]$	$[1/2^- \otimes p_{3/2}]$	$[7/2^- \otimes p_{3/2}]$
std-PRM	-0.137	0.124	0.610	0.141	0.113
def-PF	-0.137	0.033	0.756	0.146	0.055

(b) $J^\pi = 1^+$ resonant state

Model	ε (MeV)	$[3/2^- \otimes p_{3/2}]$	$[1/2^- \otimes p_{1/2}]$	$[1/2^- \otimes p_{3/2}]$	$[5/2^- \otimes p_{3/2}]$
std-PRM	0.63	0.302	0.225	0.339	0.094
def-PF	0.63	0.454	0.053	0.446	0.037

(c) $J^\pi = 3^+$ resonant state

Model	ε (MeV)	$[3/2^- \otimes p_{3/2}]$	$[7/2^- \otimes p_{1/2}]$	$[7/2^- \otimes p_{3/2}]$	$[5/2^- \otimes p_{1/2}]$	$[5/2^- \otimes p_{3/2}]$	$[9/2^- \otimes p_{3/2}]$
std-PRM	2.18	0.244	0.078	0.175	0.111	0.284	0.095
def-PF	2.18	0.579	0.030	0.364	0.000	0.012	0.000

TABLE III. The probability of $[I^\pi \otimes (\ell j)]$ in the ${}^8\text{B}$ wave functions for the (a) $J^\pi = 2^+$, (b) $J^\pi = 1^+$, and (c) $J^\pi = 3^+$ PF states (unphysical states) using the Nilsson model and the std-PRM. The lowest and the second-lowest positive-parity PF states are represented as PF1 and PF2, respectively. Only main components are listed in the tables.

(a) $J^\pi = 2^+$ PF states

State	Model	ε (MeV)	$[3/2^- \otimes p_{1/2}]$	$[3/2^- \otimes p_{3/2}]$	$[1/2^- \otimes p_{3/2}]$	$[7/2^- \otimes p_{3/2}]$	$[5/2^- \otimes p_{3/2}]$
PF1	Nilsson	-7.56	0.054	0.165	0.188	0.387	0.087
	std-PRM	-5.29	0.017	0.264	0.505	0.074	0.065
PF2	Nilsson	-7.56	0.101	0.000	0.226	0.322	0.279
	std-PRM	-4.47	0.276	0.093	0.191	0.365	0.057

(b) $J^\pi = 1^+$ PF states

State	Model	ε (MeV)	$[3/2^- \otimes p_{1/2}]$	$[3/2^- \otimes p_{3/2}]$	$[1/2^- \otimes p_{1/2}]$	$[1/2^- \otimes p_{3/2}]$	$[5/2^- \otimes p_{3/2}]$
PF1	Nilsson	-6.92	0.136	0.463	0.018	0.367	0.000
	std-PRM	-6.68	0.141	0.491	0.018	0.338	0.000
PF2	Nilsson	-6.92	0.018	0.035	0.136	0.048	0.746
	std-PRM	-2.99	0.046	0.151	0.267	0.207	0.315

(c) $J^\pi = 3^+$ PF states

State	Model	ε (MeV)	$[3/2^- \otimes p_{3/2}]$	$[7/2^- \otimes p_{1/2}]$	$[7/2^- \otimes p_{3/2}]$	$[5/2^- \otimes p_{1/2}]$	$[5/2^- \otimes p_{3/2}]$	$[9/2^- \otimes p_{3/2}]$
PF1	Nilsson	-8.37	0.495	0.153	0.304	0.004	0.026	0.000
	std-PRM	-6.67	0.752	0.086	0.136	0.001	0.008	0.000
PF2	Nilsson	-8.37	0.000	0.004	0.010	0.153	0.127	0.688
	std-PRM	1.63*	0.182	0.001	0.392	0.147	0.153	0.111

*The probabilities of this state are estimated as those of a pseudostate.

MeV, which is inconsistent with the data. For comparison, the sph-PF model is shown by the dashed line. The sph-PF model additionally yields two resonances for the 1^+ states near the first resonance with $\varepsilon_{\text{res}}(1_1^+) = 0.63$ MeV: $\varepsilon_{\text{res}}(1_2^+) = 0.68$ MeV and $\varepsilon_{\text{res}}(1_3^+) = 1.13$ MeV. These two states are primarily composed of the core-excited $I = 1/2$ component, and the corresponding peaks are not observed in the elastic or inelastic (as shown later in Fig. 6) scattering data. These results underscore the importance of excluding deformed states as PF states to precisely describe deformed halo nuclei.

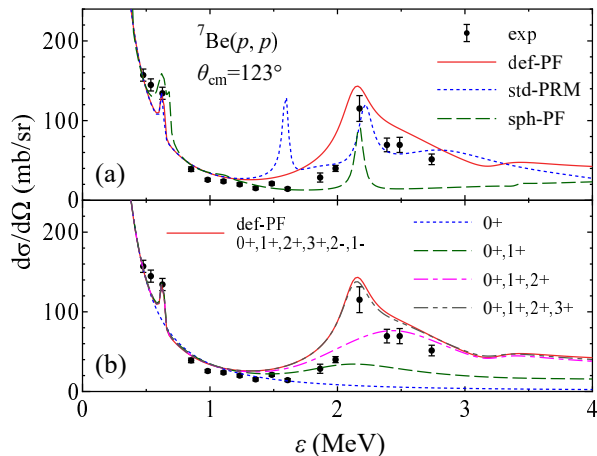


FIG. 5. Excitation function of $p + {}^7\text{Be}$ elastic scattering cross section at 123° . In (a), three models are compared: std-PRM (dotted line), def-PF model (solid line), and sph-PF model (dashed line). In (b), the J^π contributions are illustrated by expanding the model space for the def-PF model (our best result). The experimental data are taken from Ref. [46].

Finally, we apply the same model to inelastic scattering. Figure 6 presents the excitation function for $p + {}^7\text{Be}$ inelastic scattering cross section at 119° ; the line styles are the same as those used in Fig. 5. In Fig. 6(a), although the peak structure of the def-PF model (solid line) more closely approaches the experimental peak at around $\varepsilon = 2.2$ MeV than the PRM (dotted line) [see also the phase shift in Fig. 4(a)], our def-PF model does not adequately reproduce the experimental data. In Fig. 6(b), the result of the def-PF model is further decomposed into each J^π component. The decomposition reveals that the inelastic peak is mainly composed of the 2_3^+ state at $\varepsilon \approx 3.2$ MeV, which is characterized by the large core-excited component [$\mathcal{Y}_{p3/2} \otimes \phi_{1/2}$]. Although the 2^+ state could be the key to understand the behavior of inelastic scattering, further refinements of the model are required to accurately understand the complex dynamics. To preserve the simplicity of the model, we have not attempted such modifications.

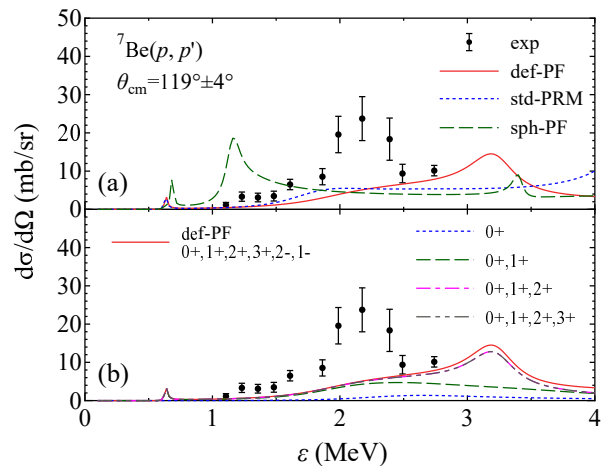


FIG. 6. Same as Fig 5, but for $p + {}^7\text{Be}$ inelastic scattering cross section at 119° . The experimental data are from Ref. [46].

IV. SUMMARY

In this study, we investigate various methods for excluding PF states in the PRM framework and evaluate their impact on the resonant-state properties. Previous studies [29, 30] introduced a simple technique for eliminating PF states in deformed halo nuclei by removing them after solving the Schrödinger equation. Despite its widespread application, our analysis reveals its limitation for ${}^8\text{B} = {}^7\text{Be} + p$, where a PF state emerges as a resonant state. To overcome this limitation, we utilize Nilsson states as PF states in the OCM, allowing us to project them out before solving the Schrödinger equation. This approach successfully reproduces the experimental data on elastic scattering excitation function, demonstrating its effectiveness. The same calculation predicts the presence of a low-energy bump in the inelastic scattering excitation function, although its position is overestimated by about 1 MeV. This result points out the need for further refinement of this model. This new approach not only overcomes the challenges encountered in ${}^8\text{B}$ calculations but also broadens the applicability to other nuclei with a deformed core, such as ${}^{17,19}\text{C}$ or ${}^{31}\text{Ne}$. The straightforward integration of this refined projectile wave function with CDCC and other reaction frameworks promises to open avenues for future research.

ACKNOWLEDGMENTS

We are grateful to P. Punta for providing the benchmark results. S.W. thanks the faculty and staff at Universidad de Sevilla for their hospitality during his sabbatical stay, which enabled the completion of this work. S.W. is supported by Japan Society for the Promotion of Science (JSPS) KAKENHI Grant No. JP22K14043. A.M.M. is supported by MCIN/AEI/10.13039/501100011033, grant

-
- [1] T. Nakamura, N. Kobayashi, Y. Kondo, Y. Satou, N. Aoi, H. Baba, S. Deguchi, N. Fukuda, J. Gibelin, N. Inabe, M. Ishihara, D. Kameda, Y. Kawada, T. Kubo, K. Kusaka, A. Mengoni, T. Motobayashi, T. Ohnishi, M. Ohtake, N. A. Orr, H. Otsu, T. Otsuka, A. Saito, H. Sakurai, S. Shimoura, T. Sumikama, H. Takeda, E. Takeshita, M. Takechi, S. Takeuchi, K. Tanaka, K. N. Tanaka, N. Tanaka, Y. Togano, Y. Utsuno, K. Yoneda, A. Yoshida, and K. Yoshida, *Phys. Rev. Lett.* **103**, 262501 (2009).
- [2] T. Nakamura, N. Kobayashi, Y. Kondo, Y. Satou, J. A. Tostevin, Y. Utsuno, N. Aoi, H. Baba, N. Fukuda, J. Gibelin, N. Inabe, M. Ishihara, D. Kameda, T. Kubo, T. Motobayashi, T. Ohnishi, N. A. Orr, H. Otsu, T. Otsuka, H. Sakurai, T. Sumikama, H. Takeda, E. Takeshita, M. Takechi, S. Takeuchi, Y. Togano, and K. Yoneda, *Phys. Rev. Lett.* **112**, 142501 (2014).
- [3] M. Takechi, T. Ohtsubo, M. Fukuda, D. Nishimura, T. Kuboki, T. Suzuki, T. Yamaguchi, A. Ozawa, T. Moriguchi, H. Ooishi, D. Nagae, H. Suzuki, S. Suzuki, T. Izumikawa, T. Sumikama, M. Ishihara, H. Geissel, N. Aoi, R.-J. Chen, D.-Q. Fang, N. Fukuda, I. Hachiuma, N. Inabe, Y. Ishibashi, Y. Ito, D. Kameda, T. Kubo, K. Kusaka, M. Lantz, Y.-G. Ma, K. Matsuta, M. Mihara, Y. Miyashita, S. Momota, K. Namihira, M. Nagashima, Y. Ohkuma, T. Ohnishi, M. Ohtake, K. Ogawa, H. Sakurai, Y. Shimbara, T. Suda, H. Takeda, S. Takeuchi, K. Tanaka, R. Watanabe, M. Winkler, Y. Yanagisawa, Y. Yasuda, K. Yoshinaga, A. Yoshida, and K. Yoshida, *Phys. Lett. B* **707**, 357 (2012).
- [4] N. Kobayashi, T. Nakamura, Y. Kondo, J. A. Tostevin, Y. Utsuno, N. Aoi, H. Baba, R. Barthelemy, M. A. Famiano, N. Fukuda, N. Inabe, M. Ishihara, R. Kanungo, S. Kim, T. Kubo, G. S. Lee, H. S. Lee, M. Matsushita, T. Motobayashi, T. Ohnishi, N. A. Orr, H. Otsu, T. Otsuka, T. Sako, H. Sakurai, Y. Satou, T. Sumikama, H. Takeda, S. Takeuchi, R. Tanaka, Y. Togano, and K. Yoneda, *Phys. Rev. Lett.* **112**, 242501 (2014).
- [5] M. Takechi, S. Suzuki, D. Nishimura, M. Fukuda, T. Ohtsubo, M. Nagashima, T. Suzuki, T. Yamaguchi, A. Ozawa, T. Moriguchi, H. Ohishi, T. Sumikama, H. Geissel, N. Aoi, R.-J. Chen, D.-Q. Fang, N. Fukuda, S. Fukuoka, H. Furuki, N. Inabe, Y. Ishibashi, T. Itoh, T. Izumikawa, D. Kameda, T. Kubo, M. Lantz, C. S. Lee, Y.-G. Ma, K. Matsuta, M. Mihara, S. Momota, D. Nagae, R. Nishikiori, T. Niwa, T. Ohnishi, K. Okumura, M. Ohtake, T. Ogura, H. Sakurai, K. Sato, Y. Shimbara, H. Suzuki, H. Takeda, S. Takeuchi, K. Tanaka, M. Tanaka, H. Uenishi, M. Winkler, Y. Yanagisawa, S. Watanabe, K. Minomo, S. Tagami, M. Shimada, M. Kimura, T. Matsumoto, Y. R. Shimizu, and M. Yahiro, *Phys. Rev. C* **90**, 061305 (2014).
- [6] P. Navrátil, R. Roth, and S. Quaglioni, *Phys. Lett. B* **704**, 379 (2011).
- [7] K. Minomo, T. Sumi, M. Kimura, K. Ogata, Y. R. Shimizu, and M. Yahiro, *Phys. Rev. Lett.* **108**, 052503 (2012).
- [8] S. Watanabe, K. Minomo, M. Shimada, S. Tagami, M. Kimura, M. Takechi, M. Fukuda, D. Nishimura, T. Suzuki, T. Matsumoto, Y. R. Shimizu, and M. Yahiro, *Phys. Rev. C* **89**, 044610 (2014).
- [9] H. Kasuya and K. Yoshida, *Prog. Theor. Exp. Phys.* **2021**, 013D01 (2020).
- [10] K. Kravvaris, P. Navrátil, S. Quaglioni, C. Hebborn, and G. Hupin, *Phys. Lett. B* **845**, 138156 (2023).
- [11] R. Takatsu, Y. Suzuki, W. Horiuchi, and M. Kimura, *Phys. Rev. C* **107**, 024314 (2023).
- [12] M. Kamimura, M. Yahiro, Y. Iseri, Y. Sakuragi, H. Kameyama, and M. Kawai, *Prog. Theor. Phys. Suppl.* **89**, 1 (1986).
- [13] N. Austern, Y. Iseri, M. Kamimura, M. Kawai, G. Rawitscher, and M. Yahiro, *Phys. Rep.* **154**, 125 (1987).
- [14] M. Yahiro, K. Ogata, T. Matsumoto, and K. Minomo, *Prog. Theor. Exp. Phys.* **2012**, 01A206 (2012).
- [15] K. Hagino, K. Ogata, and A. Moro, *Prog. Part. Nucl. Phys.* **125**, 103951 (2022).
- [16] N. C. Summers, F. M. Nunes, and I. J. Thompson, *Phys. Rev. C* **74**, 014606 (2006).
- [17] N. C. Summers, F. M. Nunes, and I. J. Thompson, *Phys. Rev. C* **89**, 069901(E) (2014).
- [18] R. de Diego, J. M. Arias, J. A. Lay, and A. M. Moro, *Phys. Rev. C* **89**, 064609 (2014).
- [19] J. A. Lay, R. de Diego, R. Crespo, A. M. Moro, J. M. Arias, and R. C. Johnson, *Phys. Rev. C* **94**, 021602(R) (2016).
- [20] R. de Diego, R. Crespo, and A. M. Moro, *Phys. Rev. C* **95**, 044611 (2017).
- [21] R. Crespo, A. Deltuva, and A. M. Moro, *Phys. Rev. C* **83**, 044622 (2011).
- [22] A. M. Moro and R. Crespo, *Phys. Rev. C* **85**, 054613 (2012).
- [23] A. M. Moro and J. A. Lay, *Phys. Rev. Lett.* **109**, 232502 (2012).
- [24] A. Deltuva, *Phys. Rev. C* **88**, 011601(R) (2013).
- [25] A. Deltuva, *Phys. Rev. C* **99**, 024613 (2019).
- [26] S. G. Nilsson, *Kgl. Dan. Mat. Fys. Medd.* **29**, 16 (1955).
- [27] I. Ragnarsson and S. G. Nilsson, *Shapes and Shells in Nuclear Structure* (Cambridge University Press, 1995).
- [28] A. Bohr and B. R. Mottelson, *Nuclear Structure* (World Scientific, Singapore, 1998).
- [29] Y. Urata, K. Hagino, and H. Sagawa, *Phys. Rev. C* **83**, 041303(R) (2011).
- [30] Y. Urata, K. Hagino, and H. Sagawa, *Phys. Rev. C* **86**, 044613 (2012).
- [31] A. Deltuva, A. Ross, E. Norvaišas, and F. M. Nunes, *Phys. Rev. C* **94**, 044613 (2016).
- [32] S. Watanabe, K. Ogata, and T. Matsumoto, *Phys. Rev. C* **103**, L031601 (2021).
- [33] P. Punta, J. A. Lay, and A. M. Moro, *Phys. Rev. C* **108**, 024613 (2023).
- [34] S. Saito, *Prog. Theor. Phys.* **40**, 893 (1968).
- [35] S. Saito, *Prog. Theor. Phys.* **41**, 705 (1969).
- [36] H. Horiuchi, *Prog. Theor. Phys. Suppl.* **62**, 90 (1977).
- [37] R. C. Johnson and P. J. R. Soper, *Phys. Rev. C* **1**, 976 (1970).

- [38] P. Descouvemont, *Comput. Phys. Commun.* **200**, 199 (2016).
- [39] P. Descouvemont and D. Baye, *Rep. Prog. Phys.* **73**, 036301 (2010).
- [40] R. Spartà, A. Di Pietro, P. Figuera, O. Tengblad, A. Moro, I. Martel, J. Fernández-García, J. Lei, L. Acosta, M. Borge, G. Bruni, J. Ced-erkäll, T. Davinson, J. Ovejas, L. Fraile, D. Galaviz, J. Halkjaer Jensen, B. Jonson, M. La Cognata, A. Perea, A. Sánchez-Benítez, N. Soić, and S. Viñals, *Phys. Lett. B* **820**, 136477 (2021).
- [41] P. Maris, M. A. Caprio, and J. P. Vary, *Phys. Rev. C* **91**, 014310 (2015).
- [42] P. Maris, M. A. Caprio, and J. P. Vary, *Phys. Rev. C* **99**, 029902(E) (2019).
- [43] J. Aguilar and J. M. Combes, *Commun. Math. Phys.* **22**, 269 (1971).
- [44] S. Aoyama, T. Myo, K. Katō, and K. Ikeda, *Prog. Theor. Phys.* **116**, 1 (2006).
- [45] E. Hiyama, Y. Kino, and M. Kamimura, *Prog. Part. Nucl. Phys.* **51**, 223 (2003).
- [46] S. N. Paneru, C. R. Brune, R. Giri, R. J. Livesay, U. Greife, J. C. Blackmon, D. W. Bardayan, K. A. Chipps, B. Davids, D. S. Connolly, K. Y. Chae, A. E. Champagne, C. Deibel, K. L. Jones, M. S. Johnson, R. L. Kozub, Z. Ma, C. D. Nesaraja, S. D. Pain, F. Sarazin, J. F. Shriner, D. W. Stracener, M. S. Smith, J. S. Thomas, D. W. Visser, and C. Wrede, *Phys. Rev. C* **99**, 045807 (2019).